Nanoporous Surface Wetting Behavior: The Line Tension Influence

V. Raspal, K. Awitor, Christophe Massard, E. Feschet-Chassot, R. Bokalawela, M. Johnson

Langmuir

Article

pubs.acs.org/Langmuir

Nanoporous Surface Wetting Behavior: The Line Tension Influence

V. Raspal,[†] K. O. Awitor,*[,†] C. Massard,[†] E. Feschet-Chassot,[†] R. S. P. Bokalawela,[‡] and M. B. Johnson[‡]

[†]C-BIOSENSS−EA 4676, Clermont Université, Université d'Auvergne, BP 10448, F-63000 Clermont-Ferrand, France

[‡]Department of Physics and Astronomy, Nielsen Hall, University of Oklahoma, 440 West Brooks, Norman, Oklahoma, 73019

ABSTRACT: The aim of this work is to develop a physical model to describe the evolution of the apparent contact angle for four different liquids on nanotextured alumina surfaces with different pore radius. The nanoporous alumina templates were fabricated by anodization of Al foil in a 0.3 M oxalic acid solution. Scanning electron microscopy was used to characterize the morphology of the surfaces. The templates are approximately 400 nm in thickness and consist of a well-ordered hexagonal array of uniform radius pores spaced 105 nm apart with pore radii from 12 to 42 nm. The wettability of nanoporous alumina templates was investigated using contact-angle measurements. We measured the contact angles using four liquids: water, ethylene glycol, aniline, and a mixture of ethylene glycol and aniline. We developed a new theoretical model for the contact angle on nanoporous surfaces as a function of the pore radius. This model is based on energy considerations and involves liquid penetration into the nanopores driven by the capillarity (Laplace's law). Because the air is compressed inside the pores, this model also includes the effect of the line tension. This is important because the three-phase line length is greatly enhanced in our nanoporous structures. For example: for a millimeter-sized droplet, the three-phase line around the perimeter of the droplet is a few millimeters long, whereas the total three-phase line within the pores can reach several tens of meters. Using our model, the line-tension value for our nanopore samples is positive and ranges from 4 to 13 × 10^{-9} N, which falls within the wide interval from 10^{-11} to 10^{-5} N quoted in the literature. Nanoporous surfaces may allow the effect of line tension to be visible for micro- to macrodroplets.

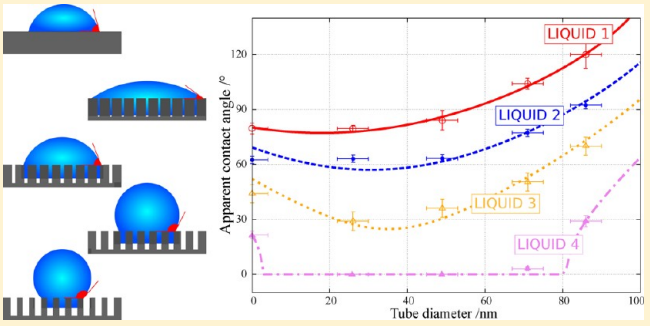

1. INTRODUCTION

Nanotextured materials are of interest in biomedical sciences. For example, modification of the surface roughness, specifically by creating nanometer-scale roughness, can trigger cell response or enhance cell adhesion.[1−7] Nanoporous alumina templates consist of well-ordered arrays of pores, where the diameter and depth of the pores can be accurately varied. Such templates are an ideal system to use for the measurement and modeling of the effect of surface roughness on the wettability of nanostructured materials, leading to a more fundamental understanding of their wetting properties. In this work, we use a cost-effective process to fabricate alumina templates that allow us to tailor their wettability. The films are approximately 400 nm in thickness and characterized by a well-ordered hexagonal array of uniform pores spaced 105 nm apart with radius from 12 to 42 nm. The template morphology was characterized using scanning electron microscopy and the wetting properties measured using contact-angle measurements with water, ethylene glycol, aniline, and a mixture of ethylene glycol and aniline. The evolution of the measured wettability of these nanoporous surfaces is compared to several theoretical models (Cassie, Wenzel, and Laplace) that are usually adequate to describe the wetting of microtextured surfaces by millimeter-sized droplets. These models do not succeed in predicting the effect of pore radius on the wetting that we observed, although they did provide important insight. We show that another term, the tension of the three-phase line (referred to as line tension), likely plays a leading role in the liquid spreading process on our nanoporous structures. This results from the fact that the length of this three-phase line is greatly enhanced in such structures. For example, for a millimeter-sized droplet, the three-phase line around the perimeter of the droplet is a few millimeters long, whereas the total three-phase line within the pores can reach several tens of meters.

The line tension has been the object of intensive work in the past decades (see Amirfazli and Neumann[8] for an excellent review). However, its physical origins and its magnitude remain poorly understood. Difficulties are encountered when trying to explain its origin in order to make a physical model, and measure its effect on the contact angle and the wettability of surfaces. The former difficulty stems from the fact that intermolecular forces are very complex to model, and the latter difficulty involves measuring the small effect of the line tension on the equilibrium parameters of the system, especially because the system size must be drastically reduced. As discussed below in our paper, the energetic surface terms dominate the volume terms below the capillarity length; similarly, the linear terms dominate the surface terms below a

Received: March 21, 2012
Revised: June 19, 2012
Published: June 29, 2012

lower characteristic length. This suggests that the line tension may play a role in the domain of biological systems. For example, it has been shown that a positive line tension can prevent the development of filopodium on a surface.[9−11]

The measurement of the line tension requires a lot of care and ingenuity in experimental design. Amirfazli and Neumann[8] sort the existing experimental methods into four main categories: thin liquid film approach,[12−15] drop-size dependence of contact angles, critical liquid lens size,[16,17] and heterogeneous nucleation.[12] For nanoporous surface wetting, a number of authors have raised issues associated with the interesting phenomena observed. Typically, the novel hydrophilic or hydrophobic properties are the result of the sample's morphology and the chemical post-treatments, and the effect of pore filling by the liquid involves the surface energy.[18−21] As far as the authors know, the line tension within a pore has not been expected to play a role. A key idea of our work is that the effect of the line tension in our nanoporous surfaces is proportional to the wetting surface area under the droplet, because a three-phase line can arise in each nanopore. This removes the requirement of the reduced size of the system to observe the effect of the line tension. To estimate the effect of the line tension, we use a model that includes the liquid penetration in the pores by capillarity and the existence of a three-phase line in the pores. A least-squares method has been applied to fit the experimental contact-angle values to get the line tensions of the liquids used.

2. EXPERIMENTAL SECTION

2.1. Fabrication of Nanoporous Alumina Templates. The nanoporous alumina templates were fabricated using a two-step anodization process on a pure (99.999%) Al foil described in detail elsewhere.[22,23] First, the 0.25-mm-thick Al foil was anodized in 0.3 M oxalic acid at 40 V and at 3 °C for 17 h to grow a thick porous oxide layer. The resulting nanoporous alumina film was then chemically stripped from the Al foil, and a secondary anodization in 0.3 M oxalic acid at 40 V and at 3 °C for 10 min was carried out. Using this two-step procedure, good pore ordering is obtained over micrometer-sized regions. The anodic aluminum oxide (AAO) films have a thickness of about 400 nm with pores of radius 12 nm spaced 105 nm apart. Pore radii can be increased by chemical etching. To do this, the pores are widened using the 0.3 M oxalic acid solution without a noticeable change in the film thickness. Pore widening is linear in time with the radius increasing about 3.3 nm per hour.

2.2. Topographic Characterization. The surface topography characterization of the alumina surfaces was performed using a Zeiss Supra 55 VP scanning electron microscope (SEM) with secondary-electron and in-lens detectors. The accelerating voltage and the working distance were 3 kV and 4 mm, respectively.

2.3. Contact-Angle Measurements. After the nanoporous surfaces were fabricated, the samples were thoroughly cleaned. Without careful cleaning, the contact-angle measurements were not repeatable. Our cleaning procedure consisted of 5 min ultrasonic baths in trichloroethylene, acetone, methanol, and finally deionized water. Then, each sample was blown dry with dry nitrogen. After this cleaning process, contact-angle measurements were consistent—repeatable for different places on a sample and for different elapsed times.

The contact-angle measurements were made using a contact-angle goniometer with a drop-shape analysis system. (Easy Drop, Kruss, Hamburg, Germany). For these measurements, a 3 μL sessile droplet was placed on a sample, under ambient conditions, with a computer-controlled syringe. Operation was monitored with the video capture system. Once equilibrium was reached, the image of the droplet profile was saved (see the right part of Figure 2) and the static apparent contact angle, $\theta^*(r)$ (or θ_Y in case of smooth surface), was measured.

3. BACKGROUND: PARAMETERS AFFECTING THE CONTACT ANGLE

When a droplet of a liquid l, surrounded by a gas phase g, is deposited on a planar solid surface s, the differential free enthalpy of the system at constant pressure and temperature is given by

$$\mathrm{d}G = mg\ \mathrm{d}z_g + \sum_i \sum_{j>i} \gamma_{ij}\ \mathrm{d}\sigma_{ij} + \tau\ \mathrm{d}\lambda \tag{1}$$

The first term is the volume energy, with m the mass of the droplet, g the gravitational acceleration, and z_g the height of the drop's center of mass. The next terms are the surface energy terms, where γ_{ij} is the surface tension (unit: N/m) between the phases i and j with area of contact σ_{ij} between the phases. (In this paper, like in most of the literature, the liquid−gas surface tension is denoted as γ.) The final term is the line-energy term, which gives the influence of the three-phase line, the line of contact between the three phases, where λ is the length and τ is the line tension (unit: N). Each of these terms depends on different powers of a characteristic length, L, of the system (L^3 for the volume, L^2 for the surface, and L for the line), so that their effect will strongly depend on the size of the droplet. The size below which surface effects dominate gravitational effects is called the capillary length: $\mathcal{L}_c = (\gamma/\rho_L\ g)^{1/2}$, where ρ_L is the density of the liquid. For water, $\mathcal{L}_c$ = 2.7 mm. Below this size, the droplet has a spherical shape and it spreads on the solid depending on the three surface tensions. For this case, the contact angle θ is then given by Young's equation[24]

$$\cos\theta_Y = \frac{\gamma_{sg} - \gamma_{sl}}{\gamma} \tag{2}$$

In the case where the solid surface is not flat, smooth, and homogeneous, a deviation of the contact angle from Young's prediction, θ_Y, is observed and explained by eq 1, still involving surface-energy terms. Two different behaviors were described by Cassie and Wenzel. The Cassie equation addresses the problem of inhomogeneity of the surface and predicts a global contact angle, θ_C, as a combination of Young's contact angles for each pure solid, θ_{Yi},[25] whereas the Wenzel equation deals with the roughness of the surface, ρ, and gives a contact angle θ_W.[26]

$$\cos\theta_C = \sum_i f_i \cos\theta_{Yi} \tag{3}$$

$$\cos\theta_W = \rho \cos\theta_Y \tag{4}$$

The Cassie equation is appropriate to model the apparent contact angle in the case where the liquid does not penetrate inside the solid asperities at all, so the contact is mixed: solid−liquid and liquid−gas. The Wenzel equation is appropriate to model the case where the liquid completely fills the pores.

In contrast to the capillary length ($\mathcal{L}_c$) and the surface tension, the characteristic length of action of the line tension (termed the line-tension length, $\mathcal{L}_t$) and the line tension are less understood and more controversial. This length is given by

$$\mathcal{L}_t = \frac{\tau}{\gamma} \tag{5}$$

and requires the knowledge of the line tension, τ. Whether the line tension is found by experiment or by theoretical models, the values of τ reported in the literature generally vary between 10^{-11} and 10^{-5} N, with disagreement on the sign.[14,15,27−33] For

dx.doi.org/10.1021/la301201k | Langmuir 2012, 28, 11064−11071

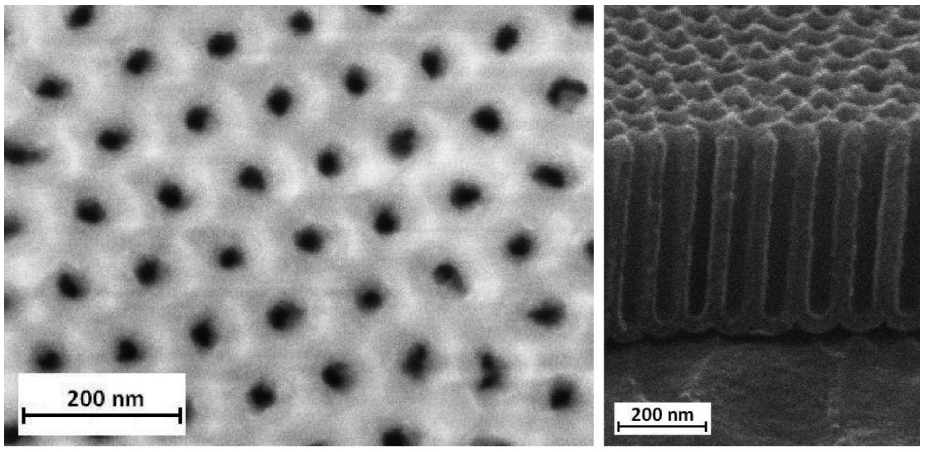

(a) Top view (b) Oblique-angle view

Figure 1. SEM images of nanoporous alumina templates.

an order of magnitude of γ around 10^{-2} N/m, $\mathcal{L}_t$ will not exceed 0.1 mm. Below this size, the effects of the line tension become significant. This upper limit on $\mathcal{L}_t$ indicates that seeing the effect of the line tension involves working with micrometer-sized droplets. However, as discussed below, we suggest that, for highly porous surfaces, where the air can be trapped in the pores, the effect of line tension can be seen even for millimeter-sized drops.

Below a given droplet size, determined by the magnitude of $\mathcal{L}_t$, the three-phase line is expected to play a role in the equilibrium of the droplet. The energetic analysis leads to a modification of Young's equation[12]

$$\cos\theta_t = \cos\theta_Y - \frac{\tau/\gamma}{R} \tag{6}$$

where θ_t is the new contact angle and R represents the radius of the solid−liquid contact area. A positive value of τ means that the three-phase line is unfavorable (it has a positive energy cost) and the droplet will limit its spreading as much as possible so that the length is reduced: the contact angle is increased. A negative value has the opposite effect. Equation 6 supports the fact that the line-tension role is hidden as long as R is much greater than $\mathcal{L}_t$. Equations 3, 4, and 6 can be combined to better describe a real system.

4. RESULTS AND DISCUSSION

4.1. Experimental Results. Figure 1a is a top-down view SEM image showing the ordered array of hexagonal pore structure in the nanoporous alumina template. Figure 1b is an oblique-angle view of the template from which we measure the template thickness to be about 400 nm.

A set of five different AAO surfaces were used. The first sample is a flat, smooth alumina surface, while the other four are surfaces with increasing pore radius obtained using longer pore widening times (see Table 1). The left part of Figure 2 shows SEM images of a few of these surfaces. These pictures indicate pore regularity with a good hexagonal distribution and the increase of pore radius. Some variation in pore radius and shape is observed. We estimate the uncertainty in pore radius to be ±2 nm.

From these different surfaces, contact-angle measurements were performed with four different liquids. Sequentially,

Table 1. Effect of Pore-Widening Chemical Etching Duration on Pore Radius and the Measured Contact Angle Values for Water and Aniline

		θ* (deg)			
pore widening time	pore radius (nm)	water	EG	EG:An (3:1)	aniline
smooth	no pores	80 ± 3	62 ± 2	44 ± 5	25 ± 2
0 h	12 ± 2	80 ± 2	63 ± 2	29 ± 5	0 ± 0
3 h	25 ± 2	85 ± 5	63 ± 2	36 ± 5	0 ± 0
6 h	37 ± 2	104 ± 3	77 ± 2	50 ± 5	3 ± 1
8 h	42 ± 2	120 ± 8	92 ± 2	70 ± 5	29 ± 2

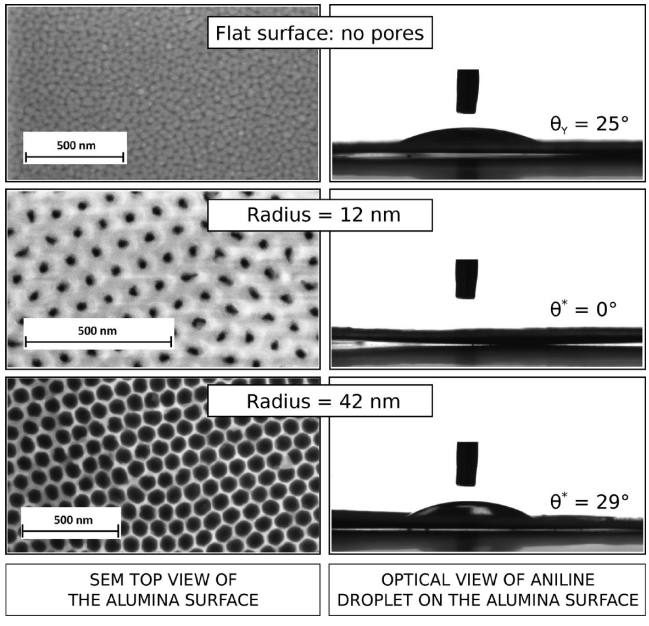

Figure 2. Left: Top-view SEM images of different kinds of alumina surfaces: flat and 12 and 42 nm pore radii. Right: Optical side-view of aniline droplets on top of corresponding alumina surfaces.

deionized water, ethylene glycol (EG), aniline, and a mixture [ethylene glycol/aniline] (3:1) (v/v) (EG:An(3:1)) were used. The right part of Figure 2 shows optical images of aniline droplets on three different alumina surfaces. The contact angles are tabulated in Table 1. For each sample and each liquid, a

dx.doi.org/10.1021/la301201k | Langmuir 2012, 28, 11064−11071

droplet was placed in three different places and the contact angle was measured. The choice of a 3 μL volume ensures that gravity has negligible influence on the shape of the droplet. (All capillary lengths are between that of water (2.7 mm) and that of aniline (2.1 mm), which is larger than 1.8 mm, the maximum height for a 3 μL droplet obtained for θ = 180°—an unlikely case.) The contact angle values in Table 1 are the average of the three measurements, and the estimated uncertainty is the standard deviation of the mean.

Examining the plots of experimental data shown in Figure 4, we observe that the evolution of θ^* with the pore-radius r is quite complicated. For the smallest values of r, the contact angle tends to fall. This decrease is stronger, for lower θ_Y. In the case of water (θ_Y = 80°), this decrease is very small. On the other hand, the reduction of aniline's contact angle is such that θ^* is 0° in the center of the pore radius range. Finally, regardless of the liquid, the apparent contact angle always increases when the pore radius reaches bigger values. In the next sections, we explore how well theoretical models describe this complicated behavior.

4.2. Theoretical Results. The goal of this section is to develop a model describing the evolution of the apparent contact angle θ^* over the radius of the pores that is better than Cassie and Wenzel models. We set the problem as an intermediate situation between the Cassie and Wenzel situations. This important assumption is not arbitrary. It is justified in section 4.3.1 after testing the Cassie and Wenzel models. For a droplet with radius smaller than capillarity length, we can neglect the gravitational terms. Thus, from eq 1, θ^* is determined by accounting for the surface and line tensions.

The surfaces we model have uniform pore structure (see Figure 1), so that for our calculations we only need to consider an elementary cell, around one pore opening. Such an elementary cell has an area $\mathcal{S}$, and is shown in the upper part of Figure 3 (top view). Young's equation shows that cos θ depends on the difference of the solid surface tension between the *dry state* (superscript d) and the *wet state* (superscript w) of a smooth surface. Here, we apply the same reasoning to one elementary cell. Using the surface energies of the dry cell ($\mathcal{E}^d$) and the wet cell ($\mathcal{E}^w$), we find that

$$\cos\theta^* = \frac{\mathcal{E}^d - \mathcal{E}^w}{\gamma \mathcal{S}} \tag{7}$$

where $\mathcal{E}^d$ and $\mathcal{E}^w$ are sums of terms with different origins:

$$\mathcal{E}^d = \mathcal{E}^d_o + \mathcal{E}^d_i \tag{8a}$$

$$\mathcal{E}^w = \mathcal{E}^w_o + \mathcal{E}^w_i + \mathcal{E}^w_m + \mathcal{E}^w_\lambda \tag{8b}$$

In these last two equations, subscripts o (i) refer to the outside (inside) of the nanopore, m refers to the meniscus of the liquid−gas interface in the pore, and λ refers to the contact-line contribution in the pore. These subscripts and other quantities of interest are depicted in the lower part (pore side view) of Figure 3. As the pores have a sealed end, the liquid is expected to penetrate and compress the air trapped inside. The penetration depth is h. Below this depth, the nature of the interfaces is the same when the cell is dry or wet, so that the effect of this part of the pore is not important for our models and we ignore it here. Using geometry, we find

$$\mathcal{E}^d_o - \mathcal{E}^w_o = ((\sqrt{3}/2)D^2 - \pi r^2)(\gamma_{sg} - \gamma_{sl}) \tag{9a}$$

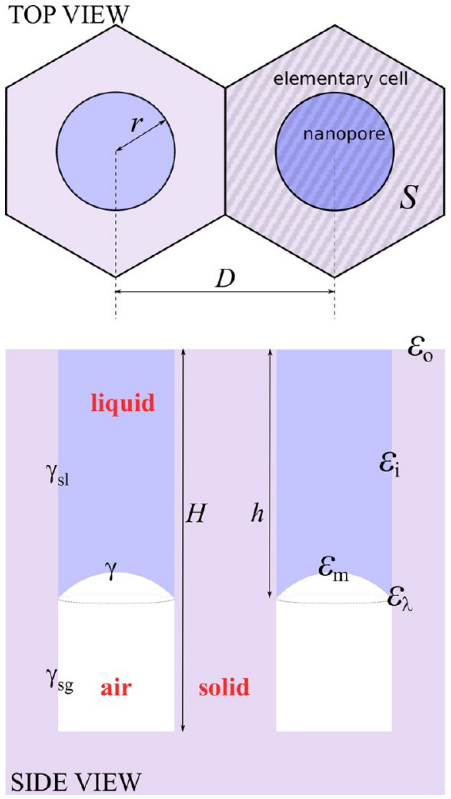

Figure 3. Top and side views of the nanopores partially filled with liquid.

$$\mathcal{E}^d_i - \mathcal{E}^w_i = 2\pi r h(\gamma_{sg} - \gamma_{sl}) \tag{9b}$$

$$\mathcal{E}^w_m = \frac{2\pi r^2}{1 + \sin\theta}\gamma \tag{9c}$$

$$\mathcal{E}^w_\lambda = 2\pi r \tau \tag{9d}$$

The surface of our elementary cell depends on the distance between adjacent pores, D, and is given by $\mathcal{S} = (\sqrt{3}/2)D^2$. Combining eqs 7 through 9, the apparent contact angle θ^* can be expressed as

$$\cos\theta^* = \left[1 + \eta\left(\frac{2h}{r} - 1\right)\right]\cos\theta_Y - \frac{2\eta}{1 + \sin\theta} - 2\eta\frac{\mathcal{L}_t}{r} \tag{10}$$

where $\eta = (2\pi/\sqrt{3})(r/D)^2$ is the surface ratio between the tube opening and the cell. The term $2\eta h/r$ is from the new contact surface between the solid and the liquid on the tube wall. It is a Wenzel-like contribution that tends to decrease θ^* in the case where the liquid wets the solid (θ_Y < 90°), which is reasonable when considering the penetration of the liquids in the pores. The term $2\eta/(1 + \sin\theta)$ comes from the liquid−gas contact inside the pore. This is a Cassie-like contribution that tends to increase θ^*. The last term in eq 10 involves the line-tension length $\mathcal{L}_t$. This term is the most interesting. It shows that the line tension contributes so as to change the apparent contact angle regardless of the size of the droplet. In such nanoporous samples, this line tension depends on L^2, not the usual L^1, so that the length of the three-phase line is proportional to the area of the wet surface. Thus, the effect of the line tension is greatly enhanced over that for nonporous samples. For the specific case of R = 1 mm, D = 100 nm, and r = 25 nm, the

dx.doi.org/10.1021/la301201k | *Langmuir* 2012, 28, 11064−11071

three-phase line around the droplet is 6.3 mm long, whereas the total three-phase line within all the pores is about 57 m long (a ratio close to 10 000:1).

The liquid penetration inside the pores originates from the capillarity phenomenon. The liquid is pushed toward the bottom of the tube by a capillary force, F_c, that is opposed by the force due to the pressure of the air trapped inside the pore, F_p. From geometry

$$F_c = 2\pi r(\gamma_{sl} - \gamma_{sg}) \tag{11a}$$

and

$$F_p = \pi r^2(P_i - P_o) \tag{11b}$$

Here, P_i is the pressure inside the pore given by

$$P_i = P_o \frac{H}{H - h} \tag{12}$$

where P_o is the pressure outside (~1 bar). The equilibrium, characterized by $F_c = F_p$, yields

$$h = \frac{2\gamma \cos\theta_Y}{2\gamma \cos\theta_Y + P_o r} H \tag{13}$$

4.3. Comparing the Models to the Experiments. In this section, we compare the apparent contact angles measured (see Table 1) with different models: (1) Cassie, (2) Wenzel, (3) Laplace (h is predicted by capillarity), and (4) modified Laplace (h is fitted). The goal is to support that the line tension likely plays an important role in the spreading of liquids on nanoporous surfaces. Finally, we show the results obtained when the model developed above, referred to as capillarity and line-tension (CLT) model, is run.

4.3.1. Cassie, Wenzel, and Laplace Models. Here, we review the behavior of the three classical models. The characteristic equation of the Cassie model based on eq 10 is

$$\cos\theta^*_C = (1 - \eta)\cos\theta_Y - \eta \tag{14}$$

The results for this model are plotted (with our data) in Figure 4A and show a global increase of θ^* for each liquid. This trend is due to the liquid−air contact that is favorable to high contact-angle values. It is clear that this model does not fit the data and the final increase of all the experimental contact angles (θ^*s) indicates that some air is trapped inside the pores.

The characteristic equation of the Wenzel model is

$$\cos\theta^*_W = \left(1 + \eta \frac{2H}{r}\right)\cos\theta_Y \tag{15}$$

where the term in parentheses is the roughness ρ. The results for this model are plotted in Figure 4B and show an abrupt decrease in the contact angle compared to the Cassie model. This decrease is due to the high roughness of our nanoporous samples, which varies as a linear function of the radius r. A simple calculation yields $\rho = 8.3$ for $H = 400$ nm and $r = 25$ nm. The Wenzel model behavior does match the observed tendency for the drop to spread more for small pore radii.

At this point, one may expect that the Laplace model may succeed in fitting the data. Indeed, this model involves the penetration of the liquid inside the pores and a compression of the air at the bottom. The characteristic equation of the Laplace model is

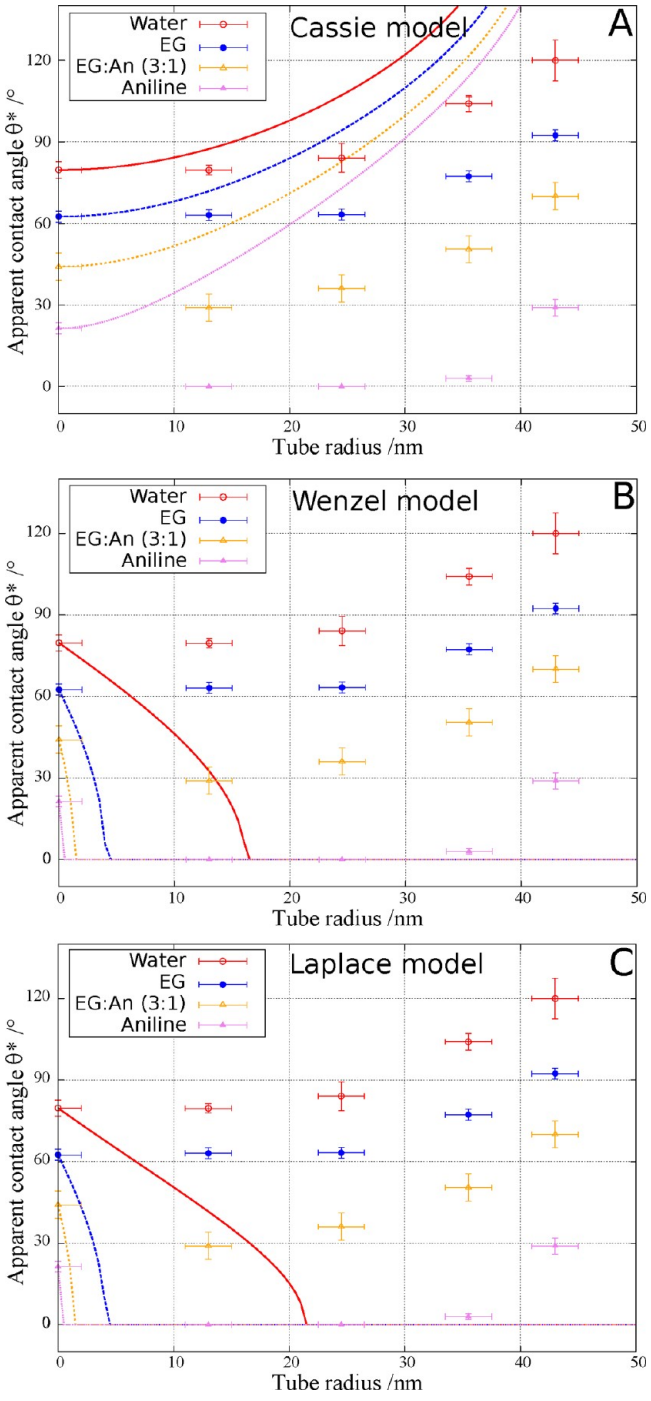

Figure 4. Solid and dashed lines: evolution of the apparent contact angle θ^* with the pore radius according to (A) Cassie model, (B) Wenzel model, and (C) Laplace model. Circles and triangles: experimental results of the contact-angle measurements for the four liquids.

$$\cos\theta^*_L = \left[1 + \eta\left(\frac{2h}{r} - 1\right)\right]\cos\theta_Y - \frac{2\eta}{1 + \sin\theta} \tag{16}$$

The results for this model are plotted (with our data) in Figure 4C. This model is called the Laplace model because Laplace's law (capillarity) is used to calculate h. Here, h is called h_{cap} and is computed with eq 13. Equation 16 combines the Wenzel and Cassie models along with their opposite trends. Unfortunately, as shown in Table 2, the nanometric size of the pores causes a

dx.doi.org/10.1021/la301201k | Langmuir 2012, 28, 11064−11071

Table 2[a]

pore radius	12 nm	25 nm	37 nm	42 nm
		h_{cap}/H		
Water	91%	84%	77%	75%
EG	95%	90%	85%	84%
EG:AN(3:1)	96%	93%	89%	88%
Aniline	97%	94%	91%	90%
		h_{cap} in nm with H = 400 nm		
Water	365	335	310	301
EG	378	359	341	335
EG:An(3:1)	385	371	358	353
Aniline	388	376	366	361

[a]Percentage filling of the nanopores for the different liquids and pore radius according to classical capillarity law. Penetration depth h_{cap} in the case H = 400 nm.

near-complete filling so that the Wenzel decreasing trend dominates the Cassie increasing trend (see Figure 4) and the results of the Laplace and Wenzel models are comparable. A smaller penetration would be expected to lead to better results.

4.3.2. Modified Laplace Model. Next, it is useful to try to find the best h value for each liquid. This is the purpose of a modified Laplace model which is based on the Laplace model (eq 16) with h no longer predicted by capillarity (h_{cap}) but set to a value called h_{fit}, where h_{fit} is set using a least-squares method to optimize the fit of the model to the experimental data. This is the "View #1" presented in Figure 6. Figure 5

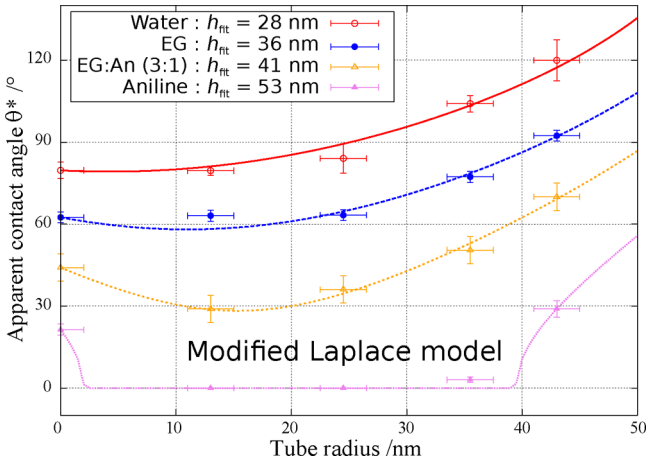

Figure 5. Solid and dashed lines: evolution of the apparent contact angle θ^* with the pore radius according to the modified Laplace model, which has the penetration depth h set to the value h_{fit} that best fits the experimental data. Circles and triangles: experimental results of the contact-angle measurements for the four liquids.

presents the plots and the penetration depth h_{fit} for each liquid. This result is encouraging: the model and experiment match well the tendencies followed by the series of liquids. However, this limitated penetration is based on a fit and is an assumption without a good physical explanation. Another more plausible view involves filling only a fraction to the depth predicted by capillarity, while the rest of the pores remain empty. This is the "View #2" presented in Figure 6. It is easier to assume a blockage at the start of the filling process (for instance, because of the high curvature around the opening) than once the filling process has proceeded. The fraction of filled pores, α, would be equivalent to the ratio h_{fit}/h_{cap}. Under this assumption and

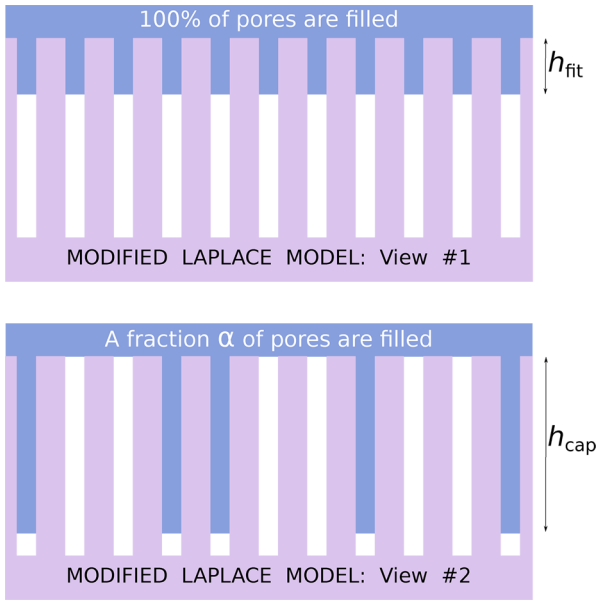

Figure 6. Two different points of view that both lead to the same spreading. View #1 assumes that liquid penetrates less (h_{fit}) than predicted by capillarity (h_{cap}). View #2 relies on an expected capillarity-filling of a limited fraction of pores α.

given that h_{cap} decreases with r (see Table 2) while h_{fit} is constant (see Figure 5), α increases slightly (see Table 3).

Table 3[a]

pore radius	12 nm	25 nm	37 nm	42 nm
Water	7.7%	8.0%	9.1%	9.3%
EG	9.5%	10.0%	11.3%	10.7%
EG:AN(3:1)	10.7%	11.0%	11.5%	11.6%
Aniline	13.7%	14.1%	14.6%	14.7%

[a]Fraction of the pores filled by the liquid by capillarity, α. The rest of pores are empty. α is computed as h_{fit}/h_{cap} so that the situation where a fraction α of the pores filled by a h_{cap} depth (View #2) is exactly equivalent to 100% of the pores filled by a h_{fit} depth (View #1).

4.3.3. Capillarity and Line-Tension (CLT) Model. The capillarity and line-tension (CLT) model, eq 10, adds the line-tension term to the Laplace model. The line tension is expected to substitute to the modifications added to the capillarity predictions in the modified Laplace model. Again, $h = h_{cap}$ in the CLT model. This extra term potentially constitutes the missing piece of the contact-angle puzzle. Figure 7 shows the resulting curves. As with the modified Laplace model, a least-squares fitting method was used to determine the value of the new parameter: the characteristic line-tension length $\mathcal{L}_t = \tau/\gamma$. Comparing the curves in Figures 5 and 7, the behavior for the modified Laplace and CLT models are similar. However, the CLT model has a physical foundation, while modified Laplace model involves an ad hoc fitting parameter. Furthermore, the close fit of the CLT model allows us to determine an important and controversial parameter value. Table 4 displays the values of $\mathcal{L}_t$, γ, and τ of each liquid. Comparison of these results with that from the literature is not easy, because line-tension values are defined for a given three-phase system that involves a different solid surface. Table 5 compares the line tension for water from the CLT model with line tensions obtained for three-phase systems that are quite

dx.doi.org/10.1021/la301201k | Langmuir 2012, 28, 11064−11071

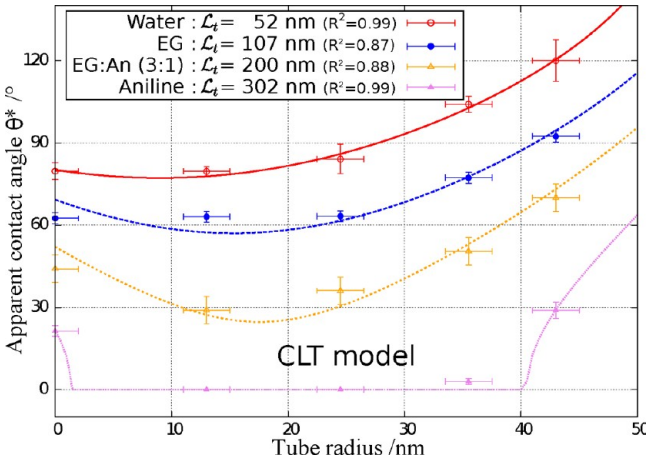

Figure 7. Solid and dashed lines: modeling of the contact angle as a function of pore radius according to the CLT model (capillarity + line tension): eq 10. The characteristic length $\mathcal{L}_t$ of the line tension of each liquid is found by a least-squares method so that the model fits the experimental data. $\mathcal{L}_t$ and the coefficient of determination R^2 are diplayed in the curve legend. Line-tension values, τ, are given in Table 4. Circles and triangles: experimental results of the contact-angle measurements for the four liquids.

Table 4. Characteristic Line-Tension Length, Surface Tension, and Line-Tension Values Found for Each Liquid

liquid	$\mathcal{L}_t$ (nm)	γ (mN·m^{-1})	τ (nN)
Water	52	73	3.8
EG	107	48	5.1
EG:An(3:1)	200	45	9.0
Aniline	302	43	13

similar to ours. We can see that, depending on the nature of the solid substrate and on the measurement technique, a wide range of values is covered. The line-tension value given by the CLT model falls within this range.

The definition used for the estimation of the coefficient of determination, R^2, is

$$R^2 = 1 - \frac{SS_{\mathrm{err}}}{SS_{\mathrm{tot}}} \tag{17}$$

where $SS_{\mathrm{err}} = \sum_i(\theta_i - \theta^*_{\mathrm{CLT}i})^2$ is the residual sum of squares and $SS_{\mathrm{tot}} = \sum_i(\theta_i - \overline{\theta_i})^2$ is the total sum of squares (proportional to variance). $\theta^*_{\mathrm{CLT}i}$ stands for the contact angle calculated with eq 10 for a radius r_i and $\overline{\theta_i}$ is the mean value of the experimental contact angles θ_i. The values obtained for the coefficient of determination range from 0.9 to 1.0. The goodness of fit supports the fact that the line tension properly solves the contact-angle problem.

4.3.4. Contribution of the Different Models. In summary, the Wenzel model indicates that there is moderate liquid penetration into the pores. The Cassie model indicates that some gas is trapped at the bottom of the tubes. The intermediate case given by the Laplace model results in a penetration that is too deep. Once modified by limiting either the penetration depth (View #1) or the ratio of filled pores (View #2), the Laplace model gives a better fit to the experimental data. However, this is solely based on fitting physical phenomena. By contrast, the CLT model mixing together capillarity and three-phase line tension delivers accurate results: a good fit and the determination of the line tension of three-phase systems that are within range of the literature.

5. CONCLUSIONS

In this paper, we explored the wetting behavior of a series of nanostructured AAO templates with 400-nm-deep pores and pore radii from 12 to 42 nm using several different solvents. The experimental data exhibits complicated contact-angle vs pore-radius behavior for these solvents. To understand this behavior, we tried to model our data using classic models including Cassie (no penetration of liquid into the pores), Wenzel (full penetration), and Laplace (partial penetration) models. These models did not match the observed behavior, although they did provide understanding, especially in the low and high porosity regions. A modified Laplace model that used the penetration depth as a fitting parameter did give good fit to the experimental data, but with no clear physical basis for the variable penetration depths. Finally, a capillarity and line-tension model (CLT), which mixes Laplace's capillarity and the physically based three-phase line tension, does fit the data very well. This should not be a surprise. Usually, pronounced effects of line tension are best observed for micro- through nanometer-sized drops, whereas we are using much larger drops. However, the structure of our nanoporous surfaces enhances the three-phase line by about 10 000 to 1, so that observing strong line-tension effects makes sense. Furthermore, the CLT-fit is sufficiently good to allow us to quantitatively determine the value of the line tension. For our alumina nanopore samples, we find line-tension values ranging from 3.8 nN for water to 13 nN for aniline. Finally, such nanopore samples provide a simple, effective alternative method to experimentally determine these difficult-to-measure line-tension values.

Table 5. Experimental Line-Tension Values from the Literature and the CLT Model

system Air−Water−...	technique	τ (N)	ref
Quartz	deformation of liquid surface	3×10^{-11}	34
Pd−C catalyst	interface coverage by particles	3×10^{-12}	35
Pd−Al_2O_3 catalyst	interface coverage by particles	5×10^{-11}	35
Pd-$BaSO_4$ catalyst	interface coverage by particles	1.5×10^{-9}	35
modified $CaCO_3$	Langmuir trough	$(1.5-2.4) \times 10^{-11}$	36
Polyethylene	contact-angle measurements	$(0.1-1) \times 10^{-8}$	30
Silicon	contact angle-measurements	$(0.6-2.3) \times 10^{-5}$	37
anodic Al_2O_3	CLT model	3.8×10^{-9}	

dx.doi.org/10.1021/la301201k | *Langmuir* 2012, 28, 11064−11071

AUTHOR INFORMATION

Corresponding Author

*E-mail address: komla.awitor@udamail.fr (K. O. Awitor).

Notes

The authors declare no competing financial interest.

ACKNOWLEDGMENTS

We acknowledge the University of Auvergne for its financial support and the NSF through C-SPIN the Oklahoma/Arkansas MRSEC (DMR-0520550).

REFERENCES

(1) Khang, D.; Lu, J.; Yao, C.; Haberstroh, K.; Webster, T. *Biomaterials* **2008**, *29*, 970−983.
(2) Park, J.; Bauer, S.; Schlegel, K.; Neukam, F.; von der Mark, K.; Schmuki, P. *Small* **2009**, *5*, 666−671.
(3) Awitor, K. O.; Rafqah, S.; Géranton, G.; Sibaud, Y.; Larson, P. R.; Bokalawela, R. S. P.; Jernigen, J. D.; Johnson, M. B. *J. Photochem. Photobiol., A* **2008**, *199*, 250−254.
(4) Vasilev, K.; Poh, Z.; Kant, K.; Chan, J.; Michelmore, A.; Losic, D. *Biomaterials* **2010**, *31*, 532−540.
(5) Puckett, S. D.; Taylor, E.; Raimondo, T.; Webster, T. J. *Biomaterials* **2010**, *31*, 706−713.
(6) Roy, S. C.; Paulose, M.; Grimes, C. A. *Biomaterials* **2007**, *28*, 4667−4672.
(7) Popat, K.; Leary Swan, E.; Mukhatyar, V.; Chatvanichkul, K.; Mor, G.; Grimes, C.; Desai, T. *Biomaterials* **2005**, *26*, 4516−4522.
(8) Amirfazli, A.; Neumann, A. *Adv. Colloid Interface Sci.* **2004**, *110*, 121−141.
(9) Lahooti, S.; Yueh, H.; Neumann, A. *Colloids Surf., B* **1995**, *3*, 333−342.
(10) Pethica, B. A. *Microbial Adhesion to Surfaces*; Lynch, J. M., Melling, J., Rutter, P. R., Vincent, B., Eds.; John Wiley & Sons: 1980; p 37.
(11) Ellwood, D. C.; Pethica, B. A. *Microbial Adhesion to Surfaces*; John Wiley & Sons: Canada, 1980; 549.
(12) Toshev, B.; Platikanov, D.; Scheludko, A. *Langmuir* **1988**, *4*, 489−499.
(13) Goodrich, F. *The Modern theory of capillarity: to the centennial of Gibbs' theory of capillarity*; Akademie-Verlag: 1981.
(14) Platikanov, D.; Nedyalkov, M.; Scheludko, A. *J. Colloid Interface Sci.* **1980**, *75*, 612−619.
(15) Platikanov, D.; Nedyalkov, M.; Scheludko, A.; Toshev, B. *J. Colloid Interface Sci.* **1988**, *121*, 100−106.
(16) Torza, S.; Mason, S. *Colloid Polym. Sci.* **1971**, *246*, 593−599.
(17) Langmuir, I. *J. Chem. Phys.* **1933**, *1*, 756.
(18) Ran, C.; Ding, G.; Liu, W.; Deng, Y.; Hou, W. *Langmuir* **2008**, *24*, 9952−9955.
(19) Lee, W.; Park, B.; Kim, D.; Ahn, D.; Park, Y.; Lee, S.; Lee, K. *Langmuir* **2009**, *26*, 1412−1415.
(20) Mateo, J.; Kulkarni, S.; Das, L.; Bandyopadhyay, S.; Tepper, G.; Wynne, K.; Bandyopadhyay, S. *Nanotechnology* **2011**, *22*, 035703.
(21) Li, Z.; Wang, J.; Zhang, Y.; Wang, J.; Jiang, L.; Song, Y. *Appl. Phys. Lett.* **2010**, *97*, 233107.
(22) Li, H.; Muller, F.; Birner, A.; Nielsch, K.; Gosele, U. *J. Appl. Phys.* **1998**, *84*, 6023.
(23) Wang, H.; Premachandran Nair, R.; Zou, M.; Larson, P. R.; Pollack, A. L.; Hobbs, K. L.; Johnson, M. B.; Awitor, O. K. *Tribol. Lett.* **2007**, *28*, 183−189.
(24) Young, T. *Phil. Trans. R. Soc. London* **1805**, 65−87.
(25) Cassie, A. *Discuss. Faraday Soc.* **1805**, 5041.
(26) Wenzel. *Ind. Eng. Chem.* **1936**, 988.
(27) Good, R.; Koo, M. *J. Colloid Interface Sci.* **1979**, *71*, 283−292.
(28) Gaydos, J.; Neumann, A. *J. Colloid Interface Sci.* **1987**, *120*, 76−86.
(29) Drelich, J.; Miller, J.; Hupka, J. *J. Colloid Interface Sci.* **1993**, *155*, 379−385.
(30) Drelich, J.; Miller, J. *J. Colloid Interface Sci.* **1994**, *164*, 252−259.
(31) Amirfazli, A.; Kwok, D.; Gaydos, J.; Neumann, A. *J. Colloid Interface Sci.* **1998**, *205*, 1−11.
(32) Chen, P.; Susnar, S.; Amirfazli, A.; Mak, C.; Neumann, A. *Langmuir* **1997**, *13*, 3035−3042.
(33) Amirfazli, A.; Hänig, S.; Müller, A.; Neumann, A. *Langmuir* **2000**, *16*, 2024−2031.
(34) Zorin, Z.; Platikanov, D.; Kolarov, T. *Colloids Surf.* **1987**, *22*, 133−145.
(35) Vinke, H.; Bierman, G.; Hamersma, P.; Fortuin, J. *Chem. Eng. Sci.* **1991**, *46*, 2497−2506.
(36) Aveyard, R.; Clint, J. *J. Chem. Soc., Faraday Trans.* **1995**, *91*, 175−176.
(37) Vera-Graziano, R.; Muhl, S.; Rivera-Torres, F. *J. Colloid Interface Sci.* **1995**, *170*, 591−597.